nature physics

SUPPLEMENTARY INFORMATION

DOI: 10.1038/NPHYS1969

The Electric Dipole Moments of the Ground State Triplet

As discussed in methods, the application of the molecular model of the centre [33] yields the electric dipole moment of the ground and excited triplet states in terms of the molecular orbitals of the centre

$$\vec{d}_{gs} \propto \frac{\lambda_1^2}{E_{es}^2}\vec{d}_{es} = \frac{\lambda_1^2}{E_{es}^2}\left(< e_x|\vec{x}|e_x > + < e_x|\vec{y}|e_y > + < a_1|\vec{z}|a_1 > + 3 < e_x|\vec{z}|e_x >\right)$$

where the molecular orbitals are defined in terms of the tetrahedrally coordinated dangling sp^3 atomic orbitals of the nearest neighbour carbon atoms of the vacancy (c_1, c_2, c_3) to be

$$a_1 = \frac{1}{\sqrt{3}\sqrt{1+2S_{cc}}}(c_1 + c_2 + c_3)$$

$$e_x = \frac{1}{\sqrt{3}\sqrt{2-2S_{cc}}}(2c_1 - c_2 - c_3)$$

$$e_y = \frac{1}{\sqrt{2-2S_{cc}}}(c_2 - c_3)$$

with $S_{cc} = < c_1|c_2 >$ being the overlap integral of the atomic orbitals. Although the molecular orbitals are approximations of the true orbitals, they provide a simple model that is qualitatively correct. Supplementary figure 1 depicts plots of the charge distributions $e_x e_x$ and $e_x e_y$ responsible for the dominant non-axial components of $\vec{d}_{es}$ and $\vec{d}_{gs}$. The plots provide a clear visualisation of the charge separations that yield the x and y components of the dipole moments.

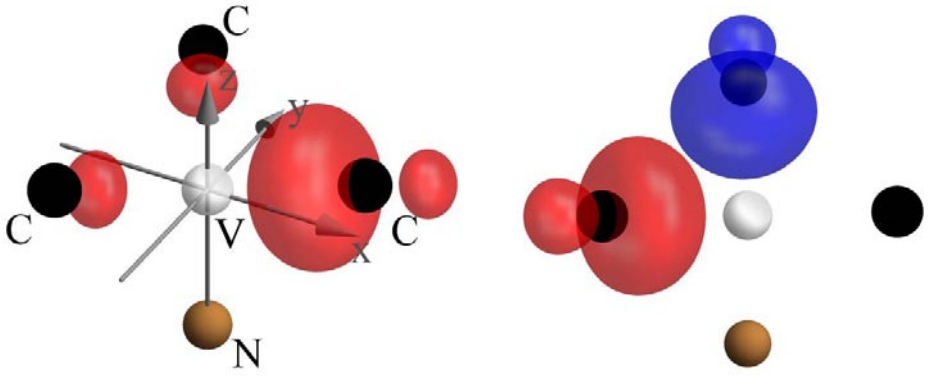

Supplementary figure 1. Electronic charge distributions responsible for the x (left) and y (right) components of the electric dipole moments of the ground and excited triplet states.The solid spheres represent the nuclei of the respective atoms neighbouring the vacancy (transparent). The positive and negative contributions to the charge distributions are red and blue respectively. The coordinate axes are defined such that the z axis coincides with the axis of symmetry connecting the nitrogen and vacancy sites.

[33] Lenef, A. & Rand, S. C. Electronic structure of the N-V center in diamond: Theory. *Physical Review B* **53**, 13441-13455 (1996).

Pulsed Optically Detected Magnetic Resonance Techniques

The electric field sensing measurements were conducted using optically detected magnetic resonance (ODMR) techniques in conjunction with applied electric and magnetic fields. The applied electric field was generated by

DOI: 10.1038/NPHYS1969

applying a controlled voltage to electrodes within a microstructure fabricated by lithography and electroplating directly on a bulk sample of diamond containing NV centres. A particular NV centre between the electrodes was selected and used for all of the measurements. The resonant microwave field used in conjunction with the optical field in implementing the ODMR techniques was generated by the gold coils adjacent to the electrodes in the microstructure with the signal carried by the outer wire and the ground plane in the inner wire. Two Helmholtz coil pairs for the x-y axes and a single coil for the z axis were used to generate and precisely manipulate the applied magnetic field (as described in methods and below). A 532 nm wavelength laser and a standard confocal arrangement were used to perform the optical spin polarization and readout of the ground state spin as part of the ODMR techniques.

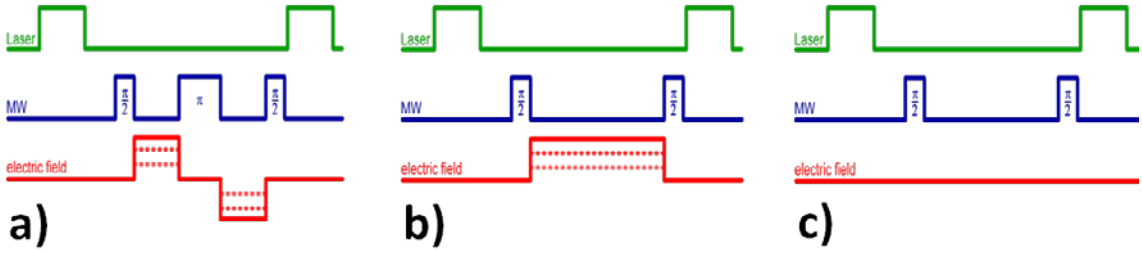

Supplementary figure 2 ODMR pulse sequences. a, Hahn echo pulse sequence used for AC electric field measurements**, b,** FID pulse sequences used for the DC electric field measurements**, c,** FID pulse sequence used to measure $\mathbf{T_2^\star}$

The AC and DC electric field measurements were conducted using Hahn echo and Free Induction Decay (FID) ODMR pulse sequences (refer to supplementary figure 2). Each sequence used an optical pulse to initialize and readout the ground state spin. The microwave pulses performed the π and $\pi/2$ rotations of the spin as part of the magnetic resonance sequences and AC and DC square voltage signals were used to generate square electric field signals between the microwave pulses. To only excite single magnetic transitions, a weak microwave signal was used, resulting in a π pulse length of a few µs. For the measurements of $T_2^\star$ a standard FID pulse sequence was used as shown in supplementary figure 2c. Note that the final microwave pulses of each sequence project the spin state into a population difference which can be detected by means of a fluorescence intensity difference (as part of the optical readout). The principle parameters of the sequences were the free evolution time between pulses τ and the voltage signal amplitude which governs the applied electric field strength.

The collected phase of the spin during the FID and Hahn echo sequences are respectively [34]

$$\Phi_{FID} = \int_0^\tau \Delta\omega(t)\, dt \quad (1)$$

and

$$\Phi_{HE} = \int_0^\tau \Delta\omega(t)\, dt - \int_\tau^{2\tau} \Delta\omega(t)\, dt \quad (2)$$

which result in different oscillating signals given by

$$\Delta I(\Delta\omega, \tau) = A\cos\Phi \quad (3)$$

For a rectangular electric field pulse shape and no phase difference between the electric field and the pulse sequence, it follows that

$$\Delta I_{FID}(\Delta\omega, \tau) = A\cos(\Delta\omega\tau) \quad (4)$$

and

$$\Delta I_{HE}(\Delta\omega, \tau) = A\cos(2\Delta\omega\tau) \quad (5)$$

Where ΔI is the amplitude change of the optically detected signal, A is the ODMR contrast, and $\Delta\omega$ is dependent on the applied electric field as detailed by (3) of the main text. For a fixed τ and an increasing $E_\perp$, an oscillation

in the detected fluorescence signal can be detected. In order to collect the maximum phase difference the alternating electric field has to be phase matched with τ so that the π pulse corresponds with the inversion of the alternating field. In order to detect an alternating field with a random phase, one has to conduct a series of measurements with the same measurement parameters, but a defined phase difference between the single measurements. From the measured phase dependent oscillations, one can determine the electric field strength. In this work only alternating fields with a perfect phase match were investigated.

[34] Mims, W. B. *The Linear Electric Field Effect in Paramagnetic Resonance*. (Clarendon Press, 1976).

Alignment of the Applied Magnetic Field

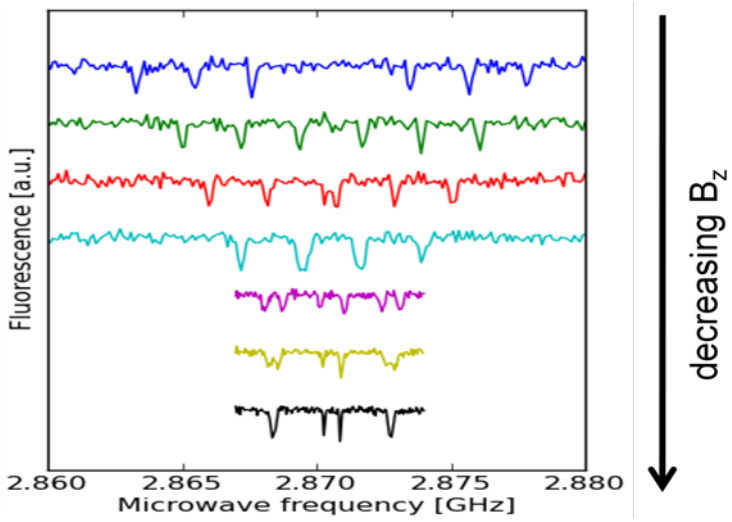

Supplementary figure 3 Continuous wave ODMR spectra used to conduct magnetic field alignment. With decreasing B_z only the central lines (m_i=0) are split by $\boldsymbol{\sigma}_\perp$. The distance between the outer lines were used to calculate the remaining B_z.

As discussed in methods, the alignment of the applied magnetic field was conducted by observing the hyperfine spectra of the centre using continuous wave ODMR techniques. Due to the small strain present in the used NV centre, the hyperfine interaction prevents a linear Stark shift of the transitions associated with the m_i=±1 states for zero B_z, thereby allowing us to use these transitions for magnetic field alignment.

For a small non-axial magnetic field $B_\perp$, the axial magnetic field is given by $B_z=\frac{\Delta\vartheta}{g\mu_B}$, where $\Delta\vartheta$ is the observed frequency difference between the m_s=0 to m_s=+1 and m_s=0 to m_s=-1 transitions. Since the hyperfine interaction creates a threefold of these transitions one has to consider the frequency difference between the lines that observe the same frequency shift due to the hyperfine interaction (e.g. $|m_s=+1\rangle|m_i=+1\rangle$ and $|m_s=-1\rangle|m_i=-1\rangle$). For zero B_z these transitions should overlap perfectly. The minimal detectable magnetic field is here determined by the line width of the observed transition. In order to align the magnetic field, we sweep the current applied to the coils, thereby sweeping B_z. In supplementary figure 3 a schematic of this sweep is shown. From interpolating the magnetic field in relation to the current in the coil, we were able to extrapolate the magnetic field values where the observed lines overlap.

For larger $B_\perp$ a simple determination of B_z is no longer possible, since the m_s=±1 states are mixed by $B_\perp$. This leads to a decrease of the observed hyperfine splitting and a decrease of the observed line shift due to B_z. Fortunately the lines still show an overlap for zero B_z, which was used to align the magnetic field in the high $B_\perp$regime. This leads to an alignment error of approx. 0.005mT and, therefore, to an error in the interaction strength of about 7percent (see figure 2b).

Reduction of T_2^* at small magnetic fields

DOI: 10.1038/NPHYS1969

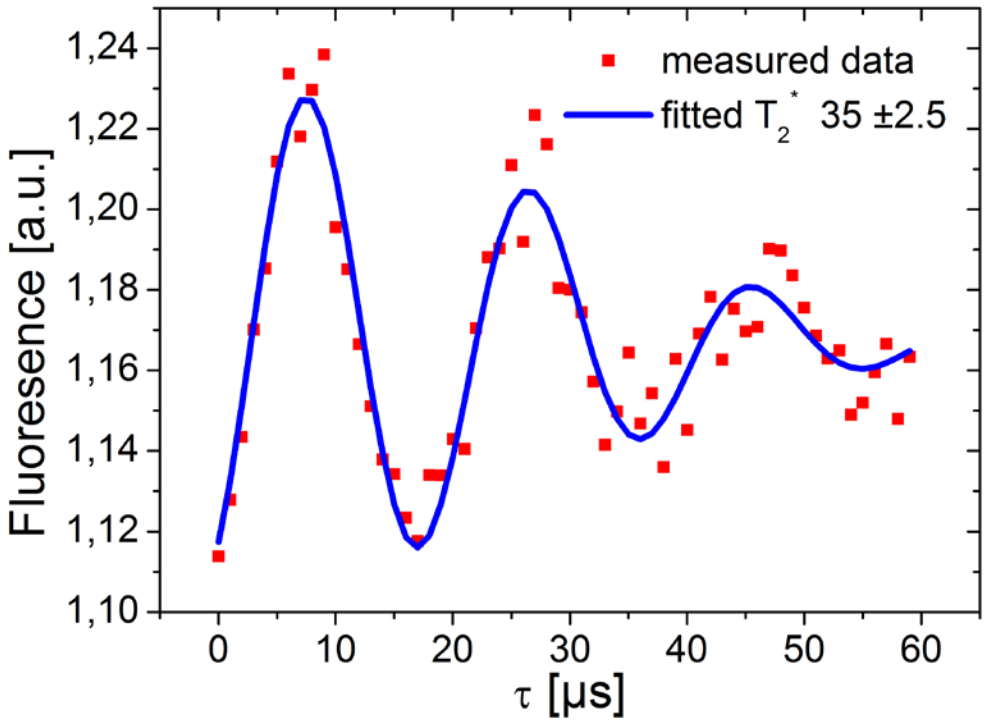

Supplementary figure 4 Example of a $\boldsymbol{T_2^*}$ measurement at $\boldsymbol{B_z}$= 0.0±0.003mT. Since only the centre transition ($\boldsymbol{m_I = 0}$) was used and the microwave frequency was carefully selected to induce an artificial detuning, a signal oscillating with the detuning frequency was measured

As depicted in the main text (figure 3d), a dependence of the NV centre's coherence time T_2^* on the axial component of the magnetic field was observed. The T_2^* clearly obtained a maximum value when the applied axial magnetic field was reduced to zero.

Given that the magnetic noise present in the diamond crystal, produced by such sources as the ^{13}C spin bath, is much greater than the electric noise, the application of an axial magnetic field reduces the T_2^* of the centre's ground state spin. The dependence of $T_2^*(B_z)$ on the axial magnetic field was modelled by the simple expression

$$T_2^*(B_z) = \kappa(B_z)\left(T_2^{*,\perp} - T_2^{*,\parallel}\right) + T_2^{*,\parallel} \quad (6)$$

where $\kappa(B_z)$ is the mixing of $|+1\rangle$ and $|-1\rangle$ as obtained from the eigenstate solution of the spin-Hamiltonian in the presence of an applied magnetic field, and $T_2^{*,\perp}$ and $T_2^{*,\parallel}$ are the coherence times for a zero axial magnetic field and a given maximum axial magnetic field $B_{z,max}$ respectively, such that $T_2^{*,\parallel} \ll T_2^{*,\perp}$. This model was used to fit the observed dependence of T_2^* as depicted in supplementary figure 3. Regardless of its simple nature, the model has produced a reasonable fit of the data. Hence, it appears that a precisely controlled magnetic field can switch the centre between regimes in which either the magnetic or electric field noise is dominant. These observations have potentially important implications for the application of the NV centre in QIP (e.g. switching the interaction between two close NVs) and decoherence imaging. Possible electric noise sources are the change of the charge state of defects by laser irradiation, fluctuating charges at the surface or any other charge fluctuations in the sample. However, in our case most of the decoherence can be attributed to noise at the electrodes. The magnetic field dependence of T_2^* was measured without connecting the electrodes.

The dependence of the electric field sensitivity on the electric, strain and magnetic fields

As detailed in (4) of the main text, the minimum detectable AC and DC applied electric fields can be expressed in terms of ΔI_{FID}, ΔI_{HE}, and the standard deviation of the signal measurement σ_{sn}, by

$$\delta E_{min}^{AC} = \sigma_{sn} \left| \frac{\partial \Delta I_{HE}}{\partial \mathrm{E}} \right|^{-1}$$

$$\delta E_{min}^{DC} = \sigma_{sn} \left| \frac{\partial \Delta I_{FID}}{\partial \mathrm{E}} \right|^{-1} \quad (8)$$

Using (4) and (5) of the supplementary information, the above expressions become

$$\delta E_{min}^{AC} = \sigma_{sn} \left| 2\mathrm{A}\tau \sin 2\Delta\omega\tau \frac{\partial \Delta\omega}{\partial \mathrm{E}} \right|^{-1}$$

$$\delta E_{min}^{DC} = \sigma_{sn} \left| \mathrm{A}\tau \sin \Delta\omega\tau \frac{\partial \Delta\omega}{\partial \mathrm{E}} \right|^{-1}$$

The minimum AC and DC applied electric fields will be detected when $|\sin 2\Delta\omega\tau| = 1$and $|\sin \Delta\omega\tau| = 1$. Defining $\tau_{HE} = (2n+1)/4\pi\Delta\omega$and $\tau_{FID} = (2n+1)/2\pi\Delta\omega$, where $n = 0,1,2\ldots$, the expression for the minimum detectable fields simplify to

$$\delta E_{min}^{AC} = \frac{\sigma_{sn}}{2\mathrm{A}\tau_{\mathrm{HE}}} \left| \frac{\partial \Delta\omega}{\partial \mathrm{E}} \right|^{-1}$$

$$\delta E_{min}^{DC} = \frac{\sigma_{sn}}{\mathrm{A}\tau_{\mathrm{FID}}} \left| \frac{\partial \Delta\omega}{\partial \mathrm{E}} \right|^{-1} \quad (9)$$

Note that τ_{HE} and τ_{FID} are limited by the T_2 andT_2^* of the NV centre respectively, which has been treated above as being independent of the strain, magnetic and the electric fields.

For the regime where the applied magnetic field is precisely aligned in the non-axial plane such that $g_e\mu_B B_z \ll g_e^2\mu_B^2 B_\perp^2/D_{gs}$, $d_{gs}^\perp \Pi_\perp \ll g_e^2\mu_B^2 B_\perp^2/D_{gs}$, and $d_{gs}^\perp \sigma_\perp \ll g_e^2\mu_B^2 B_\perp^2/D_{gs}$, the expression given for the change in the magnetic transition frequency (3) in the main text simplifies to

$$\hbar\Delta\omega \approx d_{gs}^\parallel E_z - d_{gs}^\perp \mathrm{E}_\perp \cos 2\Theta_{\mathrm{E}} - d_{gs}^\perp \sigma_\perp + d_{gs}^\perp \sigma_\perp \cos 2\phi_B \quad (10)$$

where $\Theta_{\mathrm{E}} = 2\phi_B + \phi_{\mathrm{E}}$ and the definition$\phi_\sigma = 0$ has been made. The derivatives of the changes in the magnetic transition frequencies due to the axial and non-axial electric field strengths are therefore

$$\frac{\partial \Delta\omega}{\partial \mathrm{E}_z} = \frac{\mathrm{d}_{\mathrm{gs}}^\parallel}{\hbar}$$

$$\frac{\partial \Delta\omega}{\partial \mathrm{E}_\perp} = -\frac{\mathrm{d}_{\mathrm{gs}}^\perp}{\hbar} \cos 2\Theta_{\mathrm{E}}$$

The minimum detectable axial and non-axial electric fields are then

$$\delta E_{z,min}^{AC} = \frac{\sigma_{sn}}{2\mathrm{A}\tau_{\mathrm{HE}}} \frac{\hbar}{\mathrm{d}_{\mathrm{gs}}^\parallel}$$

$$\delta E_{z,min}^{DC} = \frac{\sigma_{sn}}{\mathrm{A}\tau_{\mathrm{FID}}} \frac{\hbar}{\mathrm{d}_{\mathrm{gs}}^\parallel}$$

$$\delta E_{\perp,min}^{AC} = \frac{\sigma_{sn}}{2\mathrm{A}\tau_{\mathrm{HE}}} \frac{\hbar}{\mathrm{d}_{\mathrm{gs}}^\perp} \frac{1}{\cos 2\Theta_{\mathrm{E}}}$$

DOI: 10.1038/NPHYS1969

$$\delta E^{DC}_{\perp,min} = \frac{\sigma_{sn}}{\mathrm{A}\tau_{\mathrm{FID}}} \frac{\hbar}{\mathrm{d}^{\perp}_{\mathrm{gs}}} \frac{1}{\cos 2\Theta_{\mathrm{E}}} \quad (11)$$

It is clear that in the precisely aligned magnetic field regime, the minimum detectable electric fields do not depend on the strain, electric, and magnetic field strengths. However, the minimum detectable non-axial electric fields do depend on the relative orientation of the non-axial magnetic and electric fields. Refering to figure 2c of the main text, it is clear that the smallest detectable electric fields will occur when the non-axial magnetic field corresponds to one of the extremities of the four lobes of the plot.

In the large strain regime where $g_e \mu_B B_z \ll d^{\perp}_{gs}\sigma_{\perp}$, $g_e^2 \mu_B^2 B_{\perp}^2 / D_{gs} \ll d^{\perp}_{gs}\sigma_{\perp}$, and $\mathrm{E}_{\perp} \ll \sigma_{\perp}$, the expression given for the change in the magnetic transition frequency instead simplifies to

$$\hbar\Delta\omega \approx d^{\parallel}_{gs} E_z + d^{\perp}_{gs} \mathrm{E}_{\perp} \cos(\phi_E - \phi_\sigma) \quad (12)$$

and it follows that the minimum detectable axial and non-axial electric fields in the large strain regime are

$$\delta E^{AC}_{z,min} = \frac{\sigma_{sn}}{2\mathrm{A}\tau_{\mathrm{HE}}} \frac{\hbar}{\mathrm{d}^{\parallel}_{\mathrm{gs}}}$$

$$\delta E^{DC}_{z,min} = \frac{\sigma_{sn}}{\mathrm{A}\tau_{\mathrm{FID}}} \frac{\hbar}{\mathrm{d}^{\parallel}_{\mathrm{gs}}}$$

$$\delta E^{AC}_{\perp,min} = \frac{\sigma_{sn}}{2\mathrm{A}\tau_{\mathrm{HE}}} \frac{\hbar}{\mathrm{d}^{\perp}_{\mathrm{gs}}} \frac{1}{\cos(\phi_E - \phi_\sigma)}$$

$$\delta E^{DC}_{\perp,min} = \frac{\sigma_{sn}}{\mathrm{A}\tau_{\mathrm{FID}}} \frac{\hbar}{\mathrm{d}^{\perp}_{\mathrm{gs}}} \frac{1}{\cos(\phi_E - \phi_\sigma)} \quad (13)$$

Thus, the minimum detectable axial electric fields are the same in both regimes, whereas the minimum detectable non-axial electric fields have different dependencies on the relative orientations of the non-axial electric, magnetic and strain fields.

The two regimes offer different means to control the measurement of the electric field. In the first regime, where the magnetic field is precisely aligned in the non-axial plane, the electric field measurement can be controlled by rotating the non-axial magnetic field, as demonstrated in this work. In the second regime, where the non-axial strain dominates the effects of the other fields, the electric field measurement can be controlled by physically rotating the NV centre. Hence, the two different field regimes will be suitable to different sensor configurations and measurement conditions, thereby clearly demonstrating the flexibility of the NV centre as an electric field sensor.